Photocatalytic activity of functionalized nanodiamond-TiO_2 composites towards water pollutants degradation under UV/Vis irradiation

Pastrana-Martínez, Luisa M.; Morales-Torres, Sergio; Carabineiro, Sónia A.C.; Buijnsters, Josephus G.; Figueiredo, José L.; Silva, Adrián M.T.; Faria, Joaquim L.

DOI
10.1016/j.apsusc.2018.07.102

Publication date
2018

Document Version
Final published version

Published in
Applied Surface Science

Citation (APA)
Pastrana-Martínez, L. M., Morales-Torres, S., Carabineiro, S. A. C., Buijnsters, J. G., Figueiredo, J. L., Silva, A. M. T., & Faria, J. L. (2018). Photocatalytic activity of functionalized nanodiamond-TiO_2 composites towards water pollutants degradation under UV/Vis irradiation. *Applied Surface Science*, *458*, 839-848. https://doi.org/10.1016/j.apsusc.2018.07.102

Applied Surface Science 458 (2018) 839–848

Contents lists available at ScienceDirect

Applied Surface Science

journal homepage: www.elsevier.com/locate/apsusc

Full Length Article

Photocatalytic activity of functionalized nanodiamond-TiO_2 composites towards water pollutants degradation under UV/Vis irradiation

Luisa M. Pastrana-Martínez[a,*], Sergio Morales-Torres[a], Sónia A.C. Carabineiro[b], Josephus G. Buijnsters[c], José L. Figueiredo[b], Adrián M.T. Silva[b], Joaquim L. Faria[b]

[a] Carbon Materials Research Group, Department of Inorganic Chemistry, Faculty of Sciences, University of Granada, Campus Fuentenueva s/n, 18071 Granada, Spain
[b] Laboratory of Separation and Reaction Engineering – Laboratory of Catalysis and Materials (LSRE-LCM), Faculdade de Engenharia, Universidade do Porto, Rua Dr. Roberto Frias, 4200-465 Porto, Portugal
[c] Department of Precision and Microsystems Engineering, Research Group of Micro and Nano Engineering, Delft University of Technology, Mekelweg 2, 2628 CD Delft, The Netherlands

ARTICLE INFO

Keywords:
Nanodiamonds
TiO_2
Photocatalysis
Pharmaceutical compounds
Functionalization
Porosity

ABSTRACT

Pristine nanodiamonds (NDs) obtained by detonation, or functionalized by different treatments, namely oxidation, hydrogenation and amination, were used to synthesize composites by insertion in TiO_2 matrixes. The different treatments of the NDs lead to materials containing diverse texture properties and surface chemistry functionalities, particularly concerning the insertion of nitrogen and oxygen groups. The photocatalytic activity of the prepared composites was evaluated for the oxidative degradation of two water soluble pharmaceuticals – diphenhydramine and amoxicillin – under near-UV/Vis irradiation. The most active photocatalyst in what concerns both pollutants degradation under near-UV/Vis irradiation was the composite containing pristine NDs (NDDT). The photocatalytic performances were dependent on the specific surface area and on the amount of functional groups incorporated over the NDs. The influence of ND in the composites activity is well correlated with the observed photoluminescence quenching of TiO_2, which corresponds to a delay in the recombination rate of charge carriers that benefices the photocatalytic reaction. Scavenging of photogenerated holes and radicals by employing sacrificial hole and radical agents revealed that the holes played the main role on both pollutants degradation under UV/Vis irradiation. Reutilization experiments proved that the ND composites have good stability and reusability.

1. Introduction

Nanodiamonds (NDs) have triggered a rapidly growing interest in the materials community for a wide range of applications (such as medicine, biotechnology, electronics and catalysis) owing to their remarkable hardness, thermal conductivity, optical properties, biocompatibility and tunable surface functionalization [1]. NDs can be obtained on a large scale at low cost, by the controlled detonation of carbon-containing explosives under a negative oxygen balance. NDs produced by this method are usually called detonation NDs and were discovered in the early 1960s by Danilenko [2]. NDs are generally described by a sp^3 diamond core, surrounded by a shell composed by non-crystalline carbon that is a mixture of sp^2 and sp^3 hybridized atoms. Depending on the synthesis and post-treatments, several kinds of groups could be present on the nanoparticles surface. Normally, the surface of pristine ND particles contains a complex array of functional groups including carboxylic acids, esters, ethers, lactones, amines, among others, so several chemical modifications may be introduced in order to have a controlled surface chemistry [3,4]. After air purification or acid treatments, the NDs surface is covered by carboxylic groups. Starting from NDs with carboxylic groups, hydrogenated NDs can be obtained by treatment in hydrogen microwave CVD plasma at temperatures above 700 °C. Amination of the ND surface allows the straightforward binding of a large variety of functional molecules such as bioactive compounds or polymer building blocks by amide formation, nucleophilic attack or direct condensation reactions [5–8].

Efficient heterogeneous photocatalytic processes using modified titanium dioxide (TiO_2) particles have been amply demonstrated for environmental applications and energy conversion [9–11]. It is well known that combination of TiO_2 with carbon materials, such as graphene derivatives (i.e. graphene oxide and reduced graphene oxide) and carbon nanotubes, among others, may improve the photocatalytic

* Corresponding author.
E-mail address: lpastrana@ugr.es (L.M. Pastrana-Martínez).

https://doi.org/10.1016/j.apsusc.2018.07.102
Received 8 April 2018; Received in revised form 8 July 2018; Accepted 13 July 2018
Available online 27 July 2018
0169-4332/

activity of TiO_2 due to a synergetic interaction encompassing both interfacial electron transfer between the two constituent phases and enhanced adsorption capacity [12–15].

NDs have also stimulated the interest in the design of high-performance hybrid photocatalysts using different ND-semiconductor composites for the degradation of toluene under UV irradiation [16], degradation of water pollutants under UV/Vis and solar light irradiation [17,18], decomposition of volatile organic compounds (VOC) under visible light radiation [19] and photocatalytic hydrogen evolution reaction (HER) [20], among others.

In addition, the outstanding catalytic performance makes NDs [21], as well as composites based on graphene [22], candidates for replacing traditional metal/metal oxide catalysts in sustainable chemistry, showing their potential application as a metal free catalyst in gaseous catalytic reactions.

The introduction of surface functional groups on the ND particles plays an important role in the photocatalytic activity of the composites. It is important to refer that an oxidation treatment in air of the NDs not only produces oxygen-containing surface species (mainly carboxylic anhydrides, lactones, phenols and, in lower amounts, carbonyl/quinone groups) but also contributes to the purification of the ND powders [23,24], which leads to a marked enhancement on the photodegradation rate for the degradation of water pollutant. In our previous work, it was found that ND-TiO_2 composites were more active than those prepared with microdiamonds, in particular when NDs were oxidized in air at 430 °C, for the degradation of water pollutants under UV/Vis irradiation and solar light [17,18]. The effect of various surface modifications of NDs (oxidation, hydrogenation, graphitization and acid-purification) has been recently reported for the decomposition of VOCs using ND-loaded WO_3 composites under visible light [19]. The results showed that the activity was significantly affected by removing/increasing the graphitic layer and by the type of chemical functionalization of the surface of the ND materials [19]. In this context, there is an on-going discussion on how the incorporation of chemical functionalities would enhance the photocatalytic activity of ND-semiconductor composites.

In the present work, a series of composites were prepared with TiO_2 and commercial detonation NDs and functionalized ND samples obtained by oxidation, hydrogenation and amination, in order to investigate the role of functionalized NDs, containing different porosity and nitrogen and oxygen functionalities, on TiO_2-based composites. The photocatalytic activity of the prepared materials was assessed and discussed for the degradation of two pharmaceuticals (i.e. diphenhydramine, DP and amoxicillin, AMX) under near UV/Vis irradiation. DP ($C_{17}H_{21}NO$) is a first-generation antihistamine drug with strong resistance to biodegradation. It was selected as model pollutant because it is one of the most frequently detected pharmaceuticals in the fillet and liver of fishes [25,26]. AMX ($C_{16}H_{19}N_3O_5S$) is a semi-synthetic penicillin obtaining its antimicrobial properties from the presence of a β-lactam ring. It is widely used to treat many different types of infections caused by a wide range of Gram-positive and Gram-negative bacteria in both humans and animals [27].

2. Materials and methods

2.1. Synthesis of functionalized NDs and ND-TiO_2 composites

Carbodeon uDiamond® Molto (pristine NDD) with a primary average particle size of 5 nm was purchased from Carbodeon Ltd Oy, Vantaa (Finland). This ND powder was produced by detonation using 2,4,6-Trinitrotoluene (TNT) and 1,3,5-Trinitroperhydro-1,3,5-triazine (RDX) high explosives as precursors. Boiling acid treatment was used to remove the amorphous carbon and impurities from the detonation soot to create the purified ND powder. The following functionalized samples were obtained from the same supplier: uDiamond® Vox P (carboxyl monofunctionalized) alias oxidized NDs (NDO); uDiamond® Amine P (amine monofunctionalized) alias aminated NDs (NDA); and uDiamond® Hydrogen P (Hydrogen monofunctionalized) alias hydrogenated NDs (NDH). According to the supplier, surface chemistry conversion of the pristine ND samples was carried out in custom designed treatment plants with controlled parameters.

ND-TiO_2 composites were synthesized by liquid phase deposition adding either ND or one of the functionalized samples (NDO, NDH or NDA) to a solution containing the $(NH_4)_2TiF_6$ precursor (0.1 mol L^{-1}) and H_3BO_3 (0.3 mol L^{-1}) as described elsewhere [17]. The resulting solution was heated at 60 °C for 2 h. The amounts of NDs used in the preparation of the composite were 15.0 wt.%. The ND content was selected taking into account the best photocatalytic performance obtained with ND-TiO_2 composite in our previous work [17,18]. The solid was dried overnight and treated with N_2 at 200 °C. The composites were labelled NDDT, NDAT, NDHT and NDOT for NDD, NDA, NDH and NDO materials combined with TiO_2, respectively. For comparison, a bare TiO_2 without NDs was prepared under the same experimental conditions.

2.2. Characterization techniques

X-ray diffraction (XRD) analysis was performed in a PANalytical X'Pert MPD equipped with an X'Celerator detector and secondary monochromator (Cu Kα λ = 0.154 nm, 50 kV, 40 mA). Rietveld refinement with a PowderCell software was applied for identification of the crystallographic phases. Textural characterization of the materials was obtained from N_2 adsorption–desorption isotherms determined at −196 °C in a Quantachrome autosorb-iQ2 apparatus. The apparent surface area (S_{BET}) was determined by applying the Brunauer-Emmett-Teller (BET) equation [28], while the total pore volume (V_{pore}) was that measured at a relative pressure of 0.99. Pore size distributions (PSD) of all samples were determined by using the quenched solid density functional theory (QSDFT) [29].

The morphology of the composites was studied by scanning electron microscopy (SEM) in a FEI Quanta 400FEG ESEM/EDAX Genesis X4M instrument. High resolution transmission electron microscopy (HRTEM) observations were performed on a JEOL JEM-2100, operating at 200 kV.

The UV/Vis spectra of the solid powder materials were measured on a JASCO V-560 UV/Vis spectrophotometer equipped with an integrating sphere attachment (JASCO ISV-469). Barium sulphate was used as a reference. The spectra were recorded in diffuse reflectance mode and transformed by the instrument software to equivalent absorption Kubelka-Munk units. The band gaps of the photocatalysts were determined from the respective Tauc's plots using Kubelka–Munk units $((KM.h\nu)^{1/2})$ as a function of the energy (eV). Attenuated total reflection Fourier transform infrared (ATR-FTIR) spectra were recorded on a NICOLET 510P spectrometer using ZeSn as ATR crystal. Photoluminescence (PL) spectra were acquired using spectrofluorometer (Jasco FP-8300) with a 150 W Xenon lamp as light source, with an excitation wavelength of 330 nm and slits of 5 nm.

X-ray photoelectron spectroscopy (XPS) analysis was performed with a Kratos AXIS Ultra HSA spectrometer. The analysis was carried out with a monochromatic Al Kα X-ray source (1486.7 eV), operating at 15 kV (90 W), in FAT mode (Fixed Analyser Transmission), with a pass energy of 40 eV for regions ROI and 80 eV for survey. Data acquisition was performed with a pressure lower than 1×10^{-6} Pa, and a charge neutralization system was used. Survey and multi-region spectra were recorded at C1s, O1s and N1s photoelectron peaks. For these measurements, the binding energy (BE) values were referred to the C1s peak at 284.6 eV. Each spectral region of photoelectron interest was scanned several times to obtain good signal-to-noise ratios. The spectra obtained after a Shirley background subtraction were fitted to Lorentzian and Gaussian curves using XPS peak 4.1 software.

The point zero of charge (pH_{PZC}) of the materials was determined following a pH drift test. Briefly, N_2 was bubbled in distillate water with

the aim to prevent CO_2 dissolution and respective water acidification. Then, solutions with varying initial pH (2–12) were prepared using HCl (0.1 mol L^{-1}) or NaOH (0.1 mol L^{-1}) and 50 mL of NaCl (0.01 mol L^{-1}) as electrolyte. Each solution was contacted with 0.15 g of the material and the final pH was measured after 24 h of continuous stirring at room temperature. The PZC value of the material was determined by intercepting the obtained final-pH *vs.* initial-pH curve with the straight line final-pH = initial-pH.

2.3. Photocatalytic experiments

The photocatalytic activity of the prepared composites was evaluated for the degradation of diphenhydramine, DP ($C_{17}H_{21}NO$, 99%, Sigma-Aldrich), and amoxicillin, AMX ($C_{16}H_{19}N_3O_5S$, > 97%, Fluka) in aqueous solutions under UV/Vis irradiation at room temperature (average 25 °C). The photocatalytic experiments were performed in a cylindrical glass reactor loaded with 7.5 mL of solution containing the model pollutant DP (0.34 mM) or AMX (0.1 mM). The composite concentration was fixed as 1 g L^{-1} to avoid the effect of light scattering. The solution was magnetically stirred and continuously purged with an oxygen flow. The irradiation source consisted in a Heraeus TQ 150 medium-pressure mercury vapor lamp. A DURAN® glass cooling jacket was used for irradiation in the near-UV to visible light range (λ_{exc} = 366, 436 and 546 nm) and to maintain a room temperature in the experiments, being the photon flow reaching the photocatalytic reactor ca. 33 mW cm^{-2}, as determined by using a UV/Vis spectroradiometer (USB2000+, OceanOptics, USA). The suspension was magnetically stirred and a dark period (30 min) was maintained before switching on the lamp, in order to achieve the adsorption–desorption equilibrium condition. For all the photocatalysts tested, 30 min was proved to be enough to reach the adsorption equilibrium.

DP and AMX concentrations were determined by high performance liquid chromatography (HPLC) with a Hitachi Elite LaChrom system equipped with a Hydrosphere C18 column (250 mm × 4.6 mm), a diode array detector (L-2450) and a solvent delivery pump (L-2130). An isocratic method set at a flow rate of 1 mL min^{-1} was used with the eluent consisting of a 70% phosphate buffer solution (20 mM NaH_2PO_4 acidified with H_3PO_4 at pH 2.80) and 30% acetonitrile for DP analysis and 95% phosphate buffer solution and 5% acetonitrile for AMX analysis. Absorbance was found to be linear over the whole range considered. The total organic carbon (TOC) content of the initial and final samples was determined using a Shimadzu TOC-5000A apparatus.

3. Results and discussion

3.1. Catalysts characterization

The surface chemistry of the pristine and functionalized NDs was characterized by XPS. Fig. 1a, b and c show the deconvoluted C1s, O1s and N1s regions of the NDD, NDH, NDO and NDA samples, respectively, while the carbon (C_{XPS} %), oxygen (O_{XPS} %) and nitrogen (N_{XPS} %) contents, the fraction of species, and binding energies are listed in Table 1.

As expected, all samples show a characteristic C1s peak at 285.5 eV (Fig. 1a), which is typical of sp^3 (C—C) bonded carbon. The existence of the peak at 284.6 eV attributed to sp^2 carbon species (C=C) is mainly related to the specific surface defects in the ND surface [30]. The peaks at binding energies of ca. 286.4 and 287.7 eV, corresponding to C—O and C=O, respectively, are ascribed to the oxygenated surface groups of NDs. The surface oxygen content (Table 1) followed the order NDO > NDD > NDA > NDH, indicating that the NDO sample has the largest oxygen content (9.5 at.%), corresponding mainly to carboxylic anhydrides, lactones, phenols and carbonyl/quinones, as previously reported for NDO samples obtained by a thermal annealing in air [17]. Moreover, pristine NDs (i.e. NDD) are also found in a highly oxidized form (O_{XPS} = 6.3 at.%), as consequence likely of their production and purification procedures [31]. The XPS results also confirm that the amination and hydrogenation treatments carried out for NDA and NDH removed most of their surface oxygenated groups, decreasing the oxygen content down to 1.9 at.% and 1.8 at.%, respectively.

The XPS profiles of the ND samples differ in the amount of sp^2 carbon and the surface oxygenated groups. The lowest sp^2/sp^3 ratio was found for the pristine NDD sample (0.94). This result indicates that the surface-functionalized treatments increase the number of structural defects on the surface of the diamond nanoparticles.

The O1s spectra of the samples can be deconvoluted into three components located at ca. 529.8, 530.9 and 532.0 eV (Fig. 1b), assigned to double-bonded oxygen (C=O), single-bonded oxygen in alcohol, ether and epoxy groups C—O (1) and single-bonded oxygen in carboxyl and ester groups C—O (2).

The XPS spectrum of the N1s region of the NDD, NDH, NDO and NDA samples is shown in Fig. 1c. The presence of C—N bonds in the deconvoluted C1s spectrum overlays with the peaks assigned to C—O bonds and C—C bonds, as previously observed [32]. The XPS N1s spectra were deconvoluted into five peaks. The first peak identified at 398.7 eV, designated as N6, is attributed to pyridinic-N groups. The second peak situated at 399.9 eV is ascribed to pyrrolic-N groups (referred as N5), while the peak placed at around 401.5 eV is attributed to quaternary nitrogen (NQ) [33]. The presence of N oxides was identified in the samples by means of an additional contribution corresponding to N oxides (402.6 and 404.7 eV) [7]. The results show that N-contents in the range of about 1.5% to 2.1% were incorporated into the NDs. Similar results have been frequently reported for NDs produced by a detonation method [34–36]. The presence of nitrogen in all the ND samples may be ascribed to the occurrence of this element in the initial explosive mixture and its possible incorporation into the diamond lattice during the detonation synthesis [31,37].

The pH_{PZC} values range from 3.1 and 3.3 for NDD and NDO, respectively, to 5.2 and 4.6 for NDA and NDH, respectively. The pH_{PZC} values for ND materials increase as the oxygen content (determined by XPS) decreases (Table 1), showing that the surface of both NDA and NDH has a less acidic character.

The ATR-FTIR spectra of NDD, NDH, NDO and NDA samples are shown in Fig. 2. The main absorption bands of the functionalized ND samples are observed at ca. 1094, 1620, 1790, 2900 and 3400 cm^{-1}. The NDO spectrum shows a broad band located ca. 1094 cm^{-1} ascribed to C—O stretching vibration from anhydrides and lactones, while the band at ca. 1790 cm^{-1} is characteristic of C=O vibration in carboxylic acids, carboxylic anhydrides, quinones and lactones [18]. For the pristine NDD sample, a broad band is also obseved between 1000 and 1300 cm^{-1}, characteristic of anhydrides and lactones, possibly introduced during the ND synthesis. The broad band between 3000 and 3600 cm^{-1} and the peak at 1620 cm^{-1} are assigned to the O—H stretching and bending vibration of physisorbed water molecules and hydroxyl groups. The latter peak at ca. 1620 cm^{-1} may be also assigned to skeletal vibrations of oxidized graphitic domains (C=C). Regarding the ATR-FTIR spectra of NDH, signals located around 2900 cm^{-1} are more intense and can be assigned to C—H stretching of the hydrogenated ND surfaces, while no peaks are observed related to C=O stretching (1790 cm^{-1}) [19]. In the case of NDA, a peak around 1550 cm^{-1} ascribed to $CONH_2$ groups could be masked by the presence of the OH bond in water (1620 cm^{-1}). The C—N stretching vibration (1235–1245 cm^{-1}) is likely also not seen under the broad 1000–1300 cm^{-1} background [38].

The XRD pattern obtained from the ND samples (Fig. 3a) indicates that the powder consists of a crystalline phase, i.e., the diamond crystal lattice (identified with JCPDS card 6–675) [39]. The peaks located at 2θ = 44° and 75° correspond to diffractions from the (1 1 1) and (2 2 0) planes of cubic diamond. The average crystal size of all NDs was determined using the Scherrer equation and particle size values around 5–6 nm were calculated. The XRD patterns of the TiO_2 and ND-TiO_2

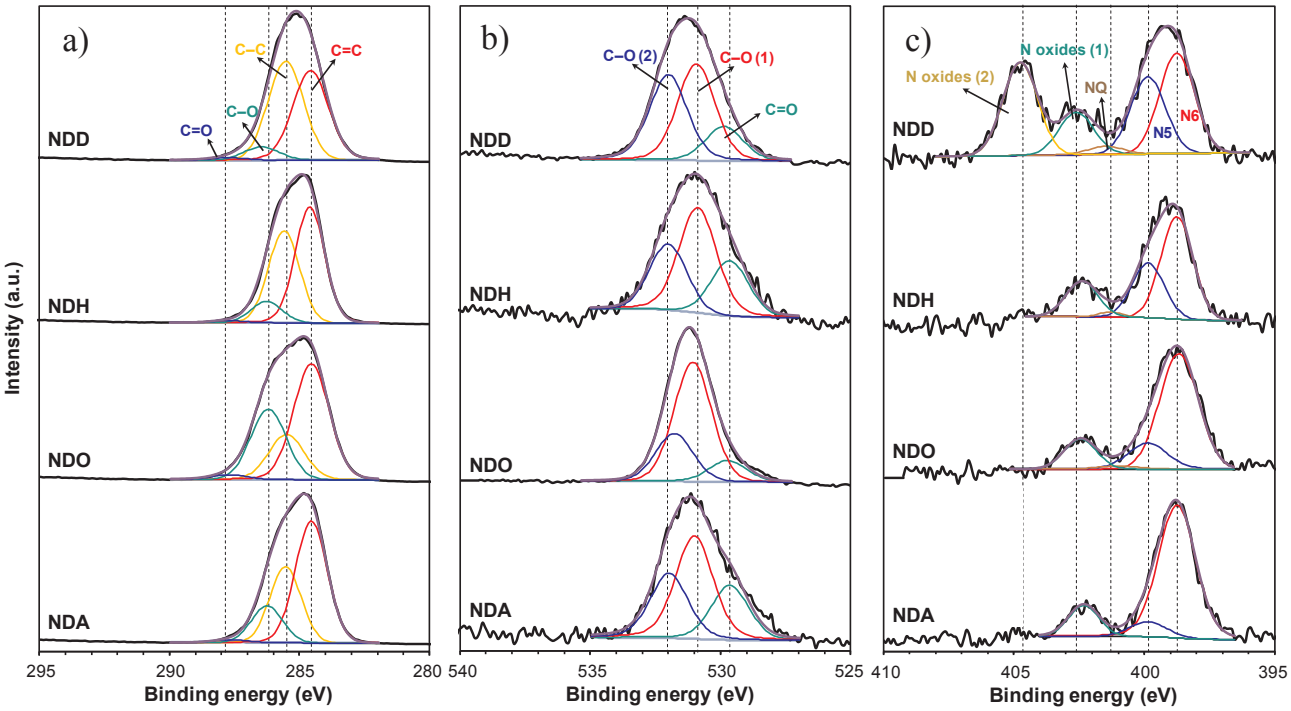

Fig. 1. XPS spectra and deconvolution of the (a) C_{1s} region, (b) O_{1s} region and (c) N_{1s} region of the different ND samples.

samples are shown in Fig. 3b. Anatase is the unique crystalline phase detected in all samples with four major diffraction peaks at 2θ values of 25.2°, 37.7°, 48.1° and 53.5° assigned to (1 0 1), (0 0 4), (2 0 0) and (1 0 5) crystal planes, respectively (JCPDS Card no. 21-1272). The crystallite size was determined by Rietveld refinement using the Williamson-Hall model (Table 2) [40]. It is observed that TiO_2 consists of anatase crystallites with an estimated size of 8.0 nm. The diffractograms of the ND-TiO_2 composites are similar to that obtained for TiO_2 (Fig. 3b) with an additional lower peak at 2θ = 44.0° attributed to the (1 1 1) plane of diamond nanocrystals as shown in Fig. 3a [18]. The anatase crystallite size of the different ND-TiO_2 composites is slightly larger than that of bare TiO_2 (up to 10.2 nm, Table 2), which could be attributed to the competition of the TiO_2 precursor species to the functionalized sites at the ND surface during the synthesis process, as previously reported [18].

Fig. 4 illustrates representative SEM images of NDD, NDH, NDO and NDA (Fig. 4a–d, respectively) and their corresponding composites (Fig. 4e–h). Bare TiO_2 (Fig. S1, Supporting Information) consists of spherical-like particles, aggregated to form larger particles. It was also possible to determine by HRTEM (not shown) that the size of TiO_2 crystallites was approximately 5 nm, and by selected-area electron diffraction SAED analysis that TiO_2 is present as anatase crystalline phase [12]. The morphology of all ND samples consists of aggregates of smaller non-spherical sub-clusters of diamond nanoparticles with edges and a broad size distribution (Fig. 4a–d for NDD, NDH, NDO and NDA, respectively). The nature of ND particles agglomeration can be due to

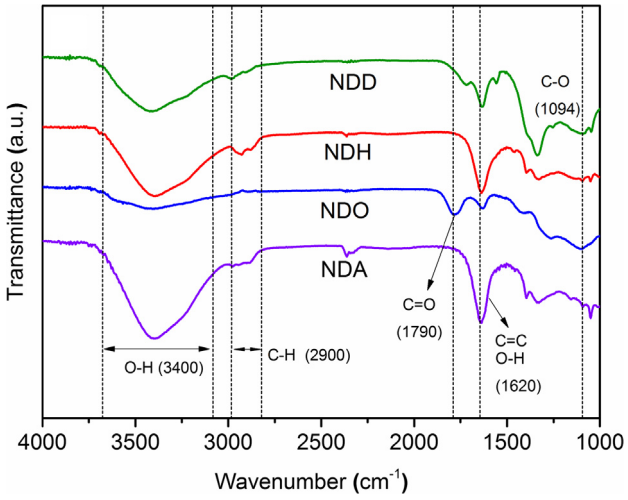

Fig. 2. ATR-FTIR spectra of the different ND samples.

Table 1
Carbon, oxygen and nitrogen contents, species percentages and corresponding binding energies (in brackets, eV) obtained by XPS analysis.

Sample	C_{XPS} at. %	O_{XPS} at. %	N_{XPS} at. %	sp^2/sp^3	C_{1s} (%)				N_{1s} (%)				
					C=C (sp^2)	C–C (sp^3)	C–O	C=O	N6	N5	NQ	N oxides	
NDD	91.6	6.3	2.1	0.94	45 (284.6)	48 (285.5)	6 (286.4)	1 (287.7)	31 (398.7)	24 (399.9)	3 (401.5)	13 (402.6)	29 (404.7)
NDH	96.7	1.8	1.5	1.25	50 (284.6)	40 (285.5)	9 (286.2)	1 (287.7)	52 (398.7)	28 (399.9)	2 (401.3)	18 (402.4)	n.d.
NDO	88.7	9.5	1.8	2.63	50 (284.6)	19 (285.5)	29 (286.2)	2 (287.7)	67 (398.7)	16 (399.9)	2 (401.1)	15 (402.4)	n.d.
NDA	96.0	1.9	2.1	1.71	53 (284.6)	31 (285.5)	15 (286.2)	1 (287.7)	78 (398.7)	8 (399.9)	n.d.	14 (402.3)	n.d.

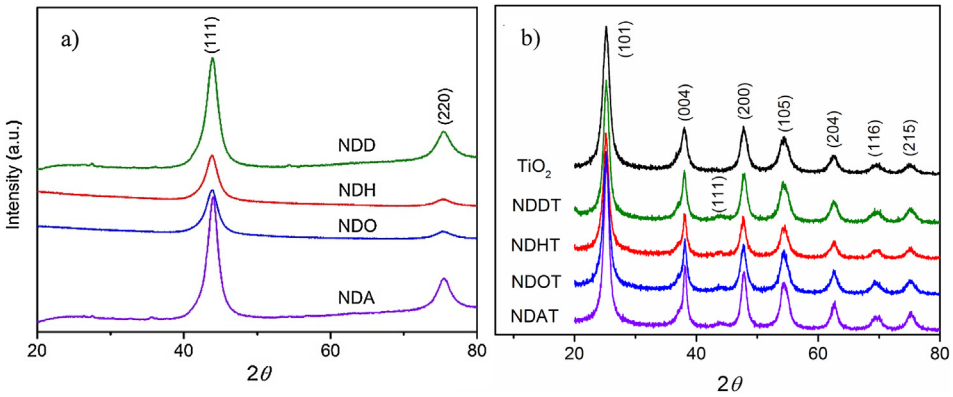

Fig. 3. XRD patterns of (a) the different ND samples and (b) TiO_2 and ND-TiO_2 composites.

Table 2
BET surface area (S_{BET}), total pore volume (V_{pore}), band-gap energy (E_g) and anatase crystallite size of TiO_2 and ND-TiO_2 composites.

Catalyst	S_{BET} ($\pm$ 5 $m^2\ g^{-1}$)	V_{pore} ($\pm$ 0.01 $cm^3\ g^{-1}$)	E_g (eV)	Anatase crystallite size (nm)
TiO_2	118	0.12	3.16	8.0 ± 0.2
NDDT	102	0.37	3.19	9.2 ± 0.2
NDHT	60	0.17	3.24	10.0 ± 0.2
NDOT	68	0.18	3.22	10.2 ± 0.2
NDAT	73	0.22	3.22	9.3 ± 0.2

van der Waals interactions, as well as the existence of hydrophilic chemical groups (such as carbonyl, carboxyl acid and lactone surface groups, among others) and sp^2 carbon residues, as previously confirmed by XPS (Fig. 1, Table 1) [41]. The SEM micrographs of the ND-TiO_2 composites show that TiO_2 grows fairly conformal to the ND particles [17] and, likely, decreasing the interactions and the aggregation of particle clusters. It is noteworthy the differences in particle size of the composite aggregates as compared to the pristine ND variants. In the case of the composites (Fig. 4, right column), the aggregates look more like clusters of 'grapes' (~100–1000 nm in size), whereas the various NDs (Fig. 4, left column) exhibit more uniform lumps.

The textural properties of all the materials were analyzed by physical adsorption of N_2 at −196 °C and the results are shown in Fig. 5. Table 2 summarizes the determined BET surface area (S_{BET}) and total pore volume (V_{pore}) of the TiO_2 and ND-TiO_2 composites. The N_2 adsorption–desorption isotherms of the ND samples and their corresponding TiO_2 composites show an adsorptive behaviour of type-II (Fig. 5a) according to the IUPAC classification [42], which is typical of macroporous materials or materials with low porosity. In general, the isotherms present a hysteresis loop of type H3, typical of non-rigid aggregates or plate-like particles, as observed by SEM (Fig. 4). The ND materials presented an apparent surface area (S_{BET}) of 242, 221, 260 and 216 $m^2\ g^{-1}$ for NDD, NDH, NDO and NDA, respectively. In all cases, the porosity of the ND materials (i.e. V_{pore} = 1.33–2.02 $cm^3\ g^{-1}$) was significantly higher than their corresponding composites (Table 2), which could be justified by the partial blockage of pores or interstitial spaces after TiO_2 assembled. The results show that NDHT, NDOT and NDAT present comparable surface area (i.e., S_{BET} = 60–73 $m^2\ g^{-1}$, Table 2) while NDDT has the highest surface area (i.e., S_{BET} = 102 $m^2\ g^{-1}$). All composites present a lower S_{BET} than that for bare TiO_2 (S_{BET} = 118 $m^2\ g^{-1}$), which could be related with the larger crystallite size obtained for the composites, as confirmed by XRD analysis (Table 2). NDDT and NDAT exhibit the highest total pore volume (V_{pore} = 0.37 and 0.22 $cm^3\ g^{-1}$ respectively), while the lowest pore volume (V_{pore} = ~0.17 $cm^3\ g^{-1}$) among the ND-TiO_2 composites was determined for NDHT and NDOT.

The pore size distributions (PSD) calculated by QSDFT to the isotherm data are shown in Fig. 5b. A blockage of pores or interstitial spaces higher than 5 nm after TiO_2 assembled was corroborated by comparing the PSD of the ND materials with their corresponding composites (Fig. 5b left *vs.* b right). It is noteworthy that the PSD of the composites mainly present mesopores of ca. 5.0 nm and micropores in a range of 1.1–1.5 nm (Fig. 5b right).

The UV–Vis absorption spectra of the ND samples are shown in Fig. S2 of the Supporting information. The results revealed a broad absorption band in the UV–Vis spectral range that can be ascribed to the colour of the powders (dark-grey), the sp^2-carbon content and a possible contribution from functional groups [43]. The DRUV–Vis spectra of TiO_2 and ND-TiO_2 composites, expressed in terms of Kubelka–Munk absorption units, are depicted in Fig. 6a. The spectra of all the samples show the characteristic absorption sharp edge rising at 400 nm in the UV region. The addition of any ND material into the TiO_2 exhibits a blue-shift on the TiO_2 absorption edge, which is attributed to the presence of localized defect states in the TiO_2 crystalline structure, as well as to the electronic semiconductor-support interaction, as previously reported [18,44]. The inset of Fig. 6a shows the Tauc's plots versus the energy of absorbed light. The value of the bare TiO_2 bandgap energy is 3.16 eV (Table 2), which is in good agreement with the theoretical value of 3.20 eV, referred for pure anatase [14]. The estimated band gap energies of NDDT, NDOT, NDAT and NDHT were found to be 3.19, 3.22, 3.22 and 3.24 eV, respectively (Table 2). The high band gap energy of ND samples (presumably around 5–6 eV) [45] when mixed with TiO_2 may constitute the major contribution for the increase of the bandgap energy of the resulting composite materials, among other aspects [18].

The Photoluminiscence (PL) emission spectra of ND samples excited at 330 nm are displayed in Fig. S3 (Supporting information). It can be observed that there are no significant differences between the photoluminescence spectrum of pristine NDD and those corresponding to the functionalized ND samples with different modified surfaces (i.e., NDO, NDA and NDH), the detected differences should be assigned apparently to different degrees of surface graphitization [46]. PL emissions of semiconductor materials are directly related to the recombination of photo-generated electrons and holes, leading to photoluminescence signals. Fig. 6b displays the PL emission spectra, excited at 330 nm, of bare TiO_2 and the ND-TiO_2 composites. The spectrum corresponding to the bare TiO_2 shows different emission bands. The strong emission band centered at ~419 nm can be due to band-band transitions for anatase TiO_2 crystal phase [47]. The observed broad band at 440–480 nm (2.58–2.82 eV) in the visible region is ascribed to the radiative recombination of excitons due to the shallow traps identified with oxygen vacancies and Ti^{4+} adjacent to oxygen vacancies [48]. The measured PL emission intensity of all ND-composites is weaker than that of bare TiO_2 (Fig. 6b). For the ND-TiO_2 composites, the order of PL intensity follows as: NDDT < NDAT < NDOT < NDHT. The weaker PL emission intensity indicates that the presence of ND materials in the

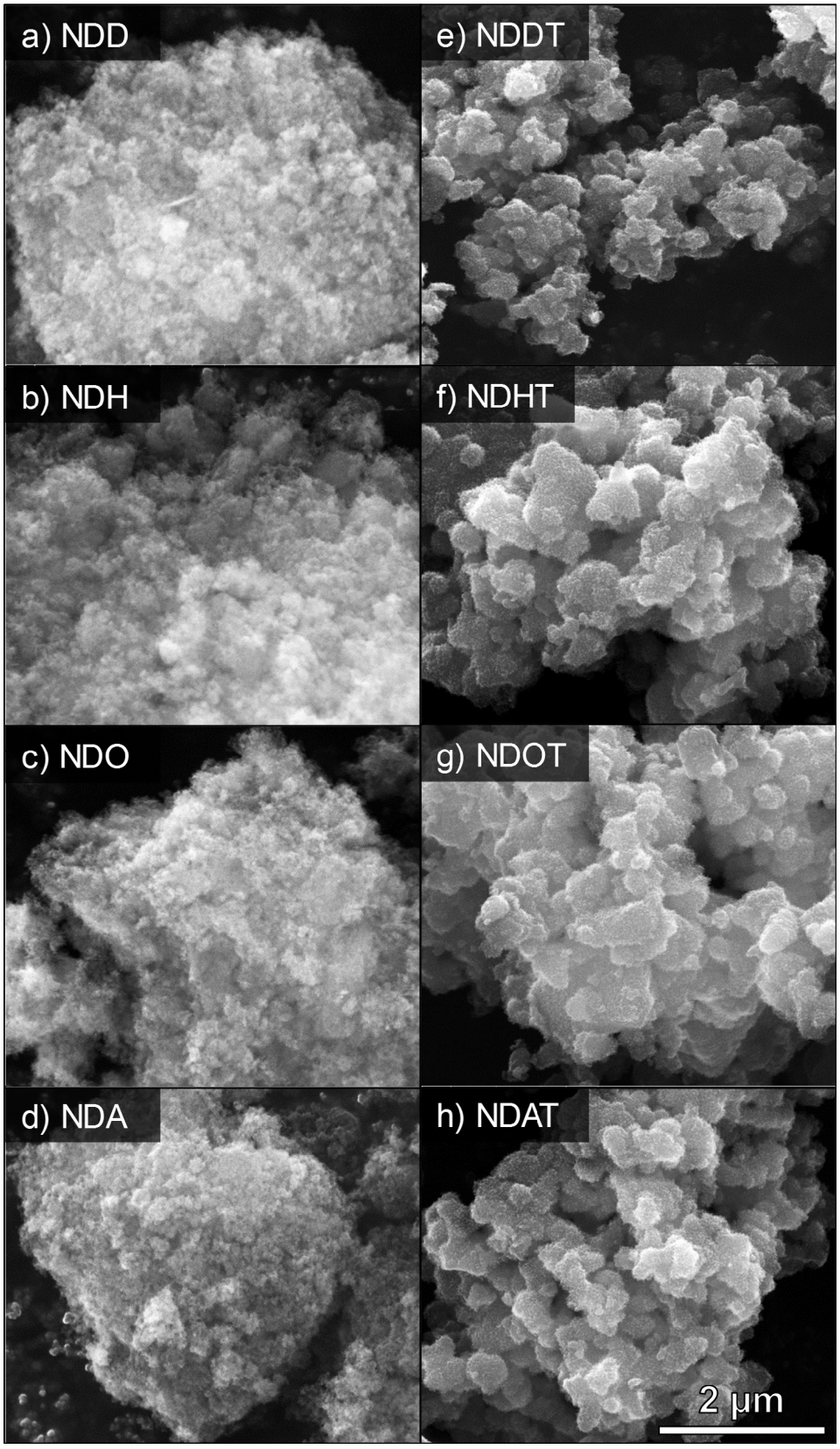

Fig. 4. SEM micrographs of (a) NDD, (b) NDH, (c) NDO, (d) NDA, (e) NDDT, (f) NDHT, (g) NDOT and (h) NDAT. Note: the common scale bar is shown at micrograph (h).

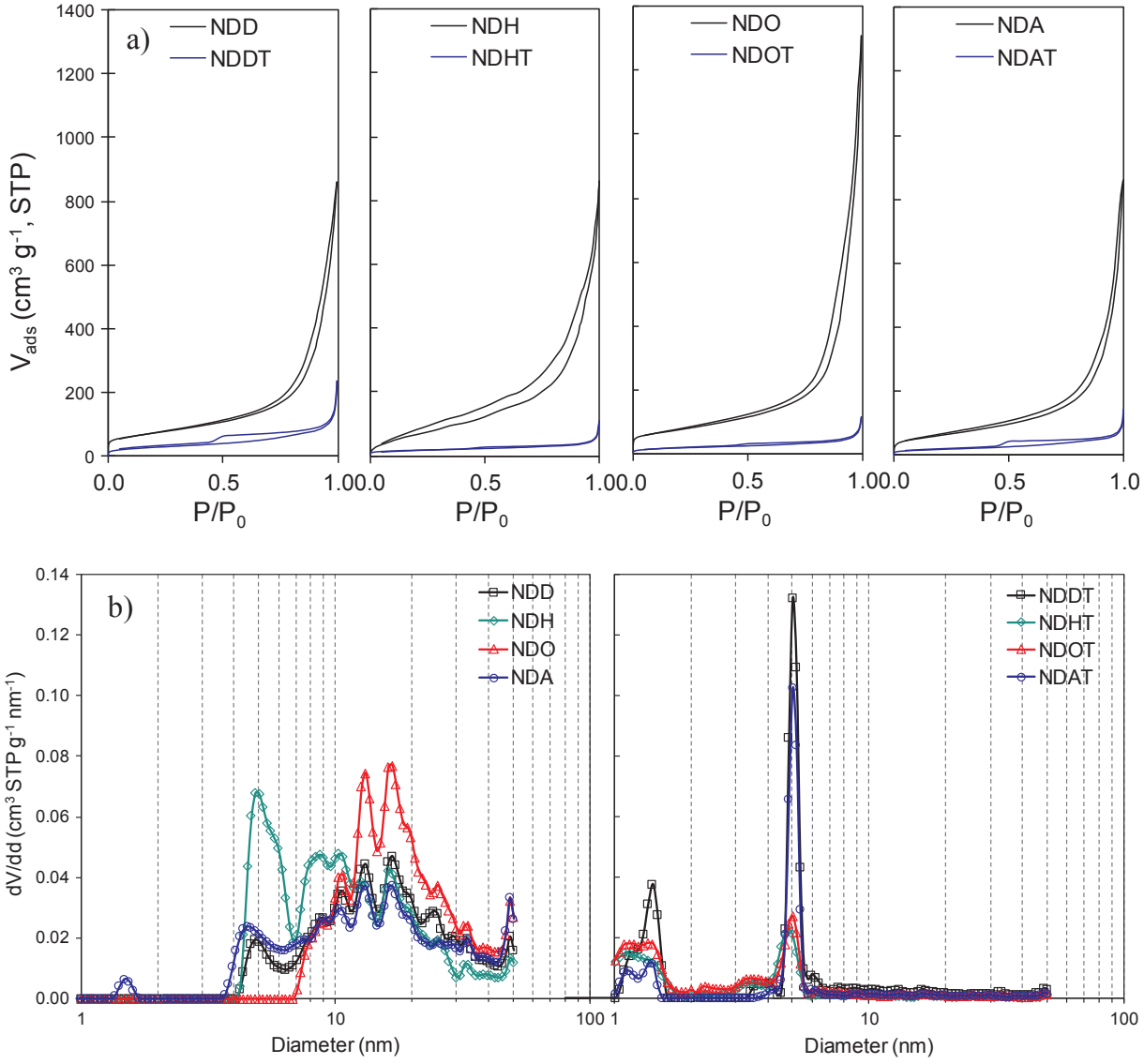

Fig. 5. (a) N_2 adsorption–desorption isotherms and (b) pore size distributions obtained by the QSDFT method for the different ND samples and their corresponding ND-TiO_2 composites.

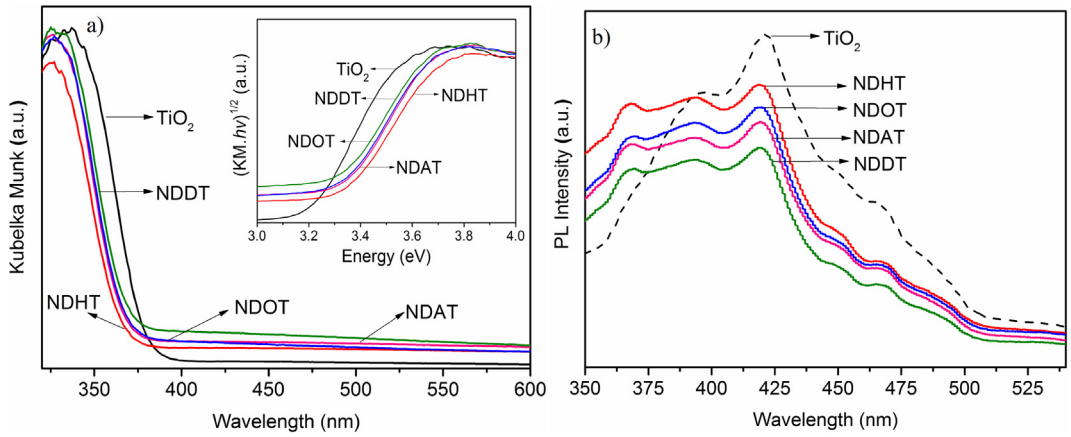

Fig. 6. (a) DRUV–Vis spectra and Tauc's plots versus the energy of adsorbed light (inset); (b) PL emission spectra (excited at a wavelength of 330 nm) of TiO_2 and ND-TiO_2 composites.

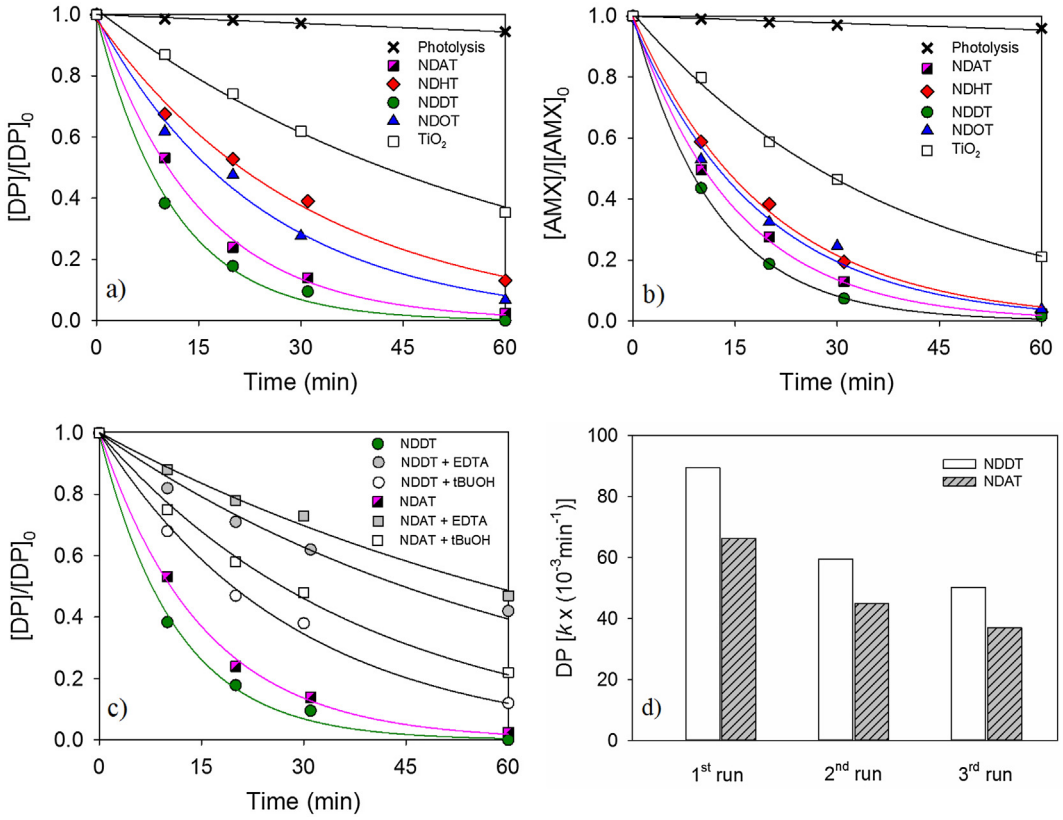

Fig. 7. Normalized concentration of (a) DP and (b) AMX as a function of time for TiO_2 and ND-TiO_2 (1.0 g L^{-1}) composites under near-UV/Vis irradiation; (c) effect of EDTA and t-BuOH on the photocatalytic degradation under near-UV/Vis irradiation of DP using NDDT and NDAT samples. Curves represent the fitting of the pseudo-first order equation to the experimental data; (d) reusability of the NDDT and NDAT samples for the DP degradation in three consecutive runs.

composites results in PL quenching, leading to a delay in the recombination rate of photogenerated charge carriers. This effect can be attributed to ND materials acting as an electron shuttle for TiO_2 to hinder electron-hole recombination, as previously observed for other carbon materials, such as graphene [49].

3.2. Photocatalytic performance of ND-TiO_2 composites

The photocatalytic efficiency of bare TiO_2 and ND-TiO_2 composites for DP and AMX degradations under near-UV/Vis irradiation is shown in Fig. 7a and b, respectively. The kinetic parameters of the time profiles are gathered in Table 3. The direct photolysis of both pollutants was first investigated in order to quantify the amount of pollutant degraded under non-catalytic conditions. The results show that both pollutants are very resistant to the photodegradation (i.e., ~5% of pollutant conversion after 60 min) in the absence of a catalyst under near-UV/Vis irradiation. On the other hand, the adsorption capacity in dark conditions was ca. 7% of the initial pollutant concentration for all photocatalysts tested. No appreciable degradation was observed for the ND materials in the absence of TiO_2 (not shown). A high photocatalytic performance for the degradation of both DP and AMX pollutants in aqueous solution was observed with all the composites under near-UV/Vis irradiation (Fig. 7a and b, respectively). It can be noticed that the presence of any ND sample variant leads to a higher pollutant degradation of the corresponding composite than that observed for the bare TiO_2 material.

For DP degradation, the photocatalytic activity of the catalysts follows the order (Fig. 7a): NDDT (90×10^{-3} min^{-1}) > NDAT

Table 3
Pseudo-first order kinetic rate constant (k) of the DP and AMX degradations and respective coefficient of variation (CV), expressed as a percentage (k_{cv}) and regression coefficient (r^2).

	Diphenhydramine (DP)			Amoxicillin (AMX)		
	k (10^{-3} min^{-1})	k_{cv} (%)	r^2	k (10^{-3} min^{-1})	k_{cv} (%)	r^2
TiO_2	16.2 ± 0.5	3.3	0.994	25.6 ± 0.5	2.2	0.997
NDDT	90 ± 4	4.2	0.997	83.3 ± 0.7	8.5	0.999
NDDT + EDTA	14.7 ± 0.8	6.1	0.991	n.d.	n.d.	n.d.
NDDT + tBuOH	35 ± 2	5.2	0.995	n.d.	n.d.	n.d.
NDHT	33 ± 1	4.4	0.992	51 ± 1	2.8	0.998
NDOT	42 ± 2	4.9	0.992	55 ± 3	6.1	0.990
NDAT	66 ± 2	2.9	0.998	67 ± 1	2.0	0.999
NDAT + EDTA	12.0 ± 0.7	6.2	0.990	n.d.	n.d.	n.d.
NDAT + tBuOH	25 ± 1	3.9	0.997	n.d.	n.d.	n.d.
Photolysis	1.00 ± 0.04	4.1	0.97	0.96 ± 0.04	3.8	0.98

n.d.: Not determined.

(66×10^{-3} min^{-1}) > NDOT (42×10^{-3} min^{-1}) > NDHT (33×10^{-3} min^{-1}) > TiO_2 (16.2×10^{-3} min^{-1}), where the values in brackets refer to the pseudo-first order rate constants (Table 3). A similar tendency was found concerning the AMX degradation under near-UV/Vis irradiation (Fig. 7b): NDDT (83.3×10^{-3} min^{-1}) > NDAT (67×10^{-3} min^{-1}) > NDOT (55×10^{-3} min^{-1}) > NDHT (51×10^{-3} min^{-1}) > TiO_2 (25.6×10^{-3} min^{-1}). These results indicate that the photocatalytic efficiencies are distinctly influenced by the type of surface functionalities incorporated on the ND materials and their porosity. Particularly, the presence of oxygen (ca. 6.3%) and nitrogen (ca. 2.1%) content on the surface of the ND samples, the high total pore volume (~0.37 cm^3 g^{-1}) as well as the boiling acid purification treatment after the detonation process likely provide superior interfacial contact between TiO_2 and the ND surface, being the composite containing pristine NDs (NDDT), the most active photocatalyst for both pollutants degradation under near-UV/Vis irradiation.

The lifetime of photogenerated charge carriers (Fig. 6b) seems to be the major contribution to justify the different photocatalytic behavior observed between the ND-TiO_2 composites towards the degradation of the organic pollutants, since the XRD patterns (Fig. 3b) and morphology of the samples (Fig. 4) are very similar. Thus, the photocatalytic results are in agreement in terms of the overall lowest PL intensity obtained for the composite based on pristine NDD (i.e. NDDT), indicating the most efficient inhibition of charge carrier recombination.

The lower photocatalytic activity observed for the composite containing NDH (NDHT) could be due to the weak interaction between TiO_2 and the hydrogen groups during the preparation method employed, as well as a slightly larger crystallite size of anatase. Therefore, NDHT presents the highest PL intensity with respect to the other composites (Fig. 6b).

The TOC removal was also determined at the end of the photocatalytic experiments for the ND-TiO_2 composites under near-UV/Vis irradiation. In general, the determined mineralization of DP showed a trend quite similar to that observed for the pollutant conversion; NDDT, NDAT, NDOT and NDHT led to TOC reductions of 18%, 15%, 11% and 11%, respectively. Therefore, NDDT presented not only the highest photocatalytic activity for DP removal, but also the highest mineralization in comparison with all other ND-TiO_2 composites tested.

The two most active ND-TiO_2 photocatalysts, i.e. NDDT and NDAT, were tested to evaluate the photocatalytic degradation pathway of the DP degradation by using 1.0 mM solutions of EDTA and tert-butanol (tBuOH) as scavengers for holes and radicals, respectively [12,50,51]. Fig. 7c shows the concentration of DP during these photocatalytic experiments in the presence of the selected scavengers. The results show that the presence of tBuOH led to a decrease of the pseudo-first order rate constants for the catalysts tested. This decrease was even more pronounced in the presence of EDTA, i.e. the pseudo-first order rate constant drops from 89.5×10^{-3} min^{-1} to 14.7×10^{-3} or 34.9×10^{-3} min^{-1} for NDDT and from 66.3×10^{-3} min^{-1} to 12.0×10^{-3} or 25.3×10^{-3} min^{-1} for NDAT in the presence of EDTA or tBuOH, respectively (Table 3). The quenching effect from tBuOH and EDTA indicates that both reactive species (such as hydroxyl, $HO^{\cdot}$, superoxide, $O_2^{\cdot -}$ and/or hydroperoxyl, $HOO^{\cdot}$ radicals) and photogenerated holes (h^+) are responsible for the photocatalytic oxidation process. However, the more pronounced decrease in the rate constant when EDTA was used, suggests that the photogenerated holes play the main role [12].

The catalyst stability of both NDDT and NDAT samples was evaluated in three utilization cycles under UV/Vis irradiation (Fig. 7d). The experimental procedure was similar to that described in Section 2.3, but in this case, after each reaction, the material was rinsed with water and dried in an oven at 80 °C for 5 h before reused in two additional consecutive photocatalytic experiments. The decrease of the rate constant between the first and the second run can be due to alteration of surface chemistry and the presence of adsorbed intermediates via strong interaction with the sp^2-conjugated carbon network of the ND surface [7] (Fig. 7d). Nevertheless, the results show quite high rate constants in the three consecutive experiments, remaining almost unchanged in the third run (50.0×10^{-3} and 37.0×10^{-3} min^{-1} for NDDT and NDAT, respectively) with respect to the second run, (59.5×10^{-3} and 45.0×10^{-3} min^{-1} for NDDT and NDAT, respectively), indicating the good stability of these materials under the applied reaction conditions.

4. Conclusions

In a series of composites prepared by insertion of detonation NDs (NDD) and NDs functionalized by oxidation (NDO), hydrogenation (NDH) and amination (NDA) in a TiO_2 matrix, it was found that the composites containing pristine NDs (NDDT) and aminated NDs (NDAT) retained the highest porosity, while having the highest atomic nitrogen composition within the surface groups (2.1 at.%). In all cases, the ND-TiO_2 composites surpassed the photocatalytic performance of the bare TiO_2 material for the degradation of two studied pharmaceuticals (i.e. diphenhydramine and amoxicillin) under near UV/Vis irradiation.

The observed photocatalytic activities are explained in terms of a better charge separation of the carriers on the photocatalysts upon photoexcitation, which was confirmed by the photoluminescence quenching measurements. The photogenerated holes play a major role in the mechanism of diphenhydramine degradation as inferred from the observed remarkable decrease in the degradation rate constant in presence of EDTA as hole scavenger.

The present report provides some important new insights for the use of ND materials (that can be obtained on a large scale in a cost-effective method) as substitute of expensive noble metal and other co-catalysts, for the degradation of organic pollutants.

Acknowledgments

This work is a result of project “AIProcMat@N2020 - Advanced Industrial Processes and Materials for a Sustainable Northern Region of Portugal 2020”, with the reference NORTE-01-0145-FEDER-000006, supported by Norte Portugal Regional Operational Programme (NORTE 2020), under the Portugal 2020 Partnership Agreement, through the European Regional Development Fund (ERDF) and of Project POCI-01-0145-FEDER-006984 – Associate Laboratory LSRE-LCM funded by ERDF through COMPETE2020 - Programa Operacional Competitividade e Internacionalização (POCI) – and by national funds through FCT - Fundação para a Ciência e a Tecnologia. SACC and AMTS acknowledge Investigador FCT (IF/01381/2013 and IF/01501/2013, respectively), with financing from the European Social Fund and the Human Potential Operational Program. LMPM acknowledges the Spanish Ministry of Economy and Competitiveness (MINECO) and the European Social Fund for a Ramon y Cajal research contract (RYC-2016-19347). SMT acknowledges the financial support from University of Granada (Reincorporación Plan Propio). Authors are thankful to Dr. Carlos M. Sá (CEMUP) for assistance with XPS analyses.

Appendix A. Supporting information

Supplementary data associated with this article can be found, in the online version, at https://doi.org/10.1016/j.apsusc.2018.07.102.

References

[1] E. Osawa, Monodisperse single nanodiamond particulates, Pure Appl. Chem. 80 (2008) 1365–1379.
[2] V.V. Danilenko, On the history of the discovery of nanodiamond synthesis, Phys. Solid State 46 (2004) 595–599.
[3] S. Osswald, G. Yushin, V. Mochalin, S.O. Kucheyev, Y. Gogotsi, Control of sp^2/sp^3 carbon ratio and surface chemistry of nanodiamond powders by selective oxidation in air, J. Am. Chem. Soc. 128 (2006) 11635–11642.
[4] A.S. Barnard, S.P. Russo, I.K. Snook, Structural relaxation and relative stability of nanodiamond morphologies, Diam. Relat. Mater. 12 (2003) 1867–1872.
[5] L. Hawelek, A. Brodka, J.C. Dore, V. Honkimaki, S. Tomita, A. Burian, Structural

studies of nanodiamond by high-energy X-ray diffraction, Diam. Relat. Mater. 17 (2008) 1186–1193.
[6] O.O. Mykhaylyk, Y.M. Solonin, D.N. Batchelder, R. Brydson, Transformation of nanodiamond into carbon onions: a comparative study by high-resolution transmission electron microscopy, electron energy-loss spectroscopy, X-ray diffraction, small-angle x-ray scattering, and ultraviolet Raman spectroscopy, J. Appl. Phys. 97 (2005) 074302.
[7] X. Duan, Z. Ao, D. Li, H. Sun, L. Zhou, A. Suvorova, M. Saunders, G. Wang, S. Wang, Surface-tailored nanodiamonds as excellent metal-free catalysts for organic oxidation, Carbon 103 (2016) 404–411.
[8] O.A. Shenderova, G.E. McGuire, Science and engineering of nanodiamond particle surfaces for biological applications (Review), Biointerphases 10 (2015) 030802.
[9] J. Schneider, M. Matsuoka, M. Takeuchi, J. Zhang, Y. Horiuchi, M. Anpo, D.W. Bahnemann, Understanding TiO_2 photocatalysis: mechanisms and materials, Chem. Rev. 114 (2014) 9919–9986.
[10] G. Liu, L.-C. Yin, J. Wang, P. Niu, C. Zhen, Y. Xie, H.-M. Cheng, A red anatase TiO_2 photocatalyst for solar energy conversion, Energy Environ. Sci. 5 (2012) 9603–9610.
[11] P. Su, H. Li, J. Wang, J. Wu, B. Zhao, F. Wang, Facile preparation of titanium dioxide nano-capsule arrays used as photo-anode for dye sensitized solar cells, Appl. Surf. Sci. 347 (2015) 636–642.
[12] L.M. Pastrana-Martínez, S. Morales-Torres, V. Likodimos, J.L. Figueiredo, J.L. Faria, P. Falaras, A.M.T. Silva, Advanced nanostructured photocatalysts based on reduced graphene oxide–TiO_2 composites for degradation of diphenhydramine pharmaceutical and methyl orange dye, Appl. Catal. B 123–124 (2012) 241–256.
[13] C.G. Silva, J.L. Faria, Photocatalytic oxidation of benzene derivatives in aqueous suspensions: synergic effect induced by the introduction of carbon nanotubes in a TiO_2 matrix, Appl. Catal. B 101 (2010) 81–89.
[14] X. Li, R. Shen, S. Ma, X. Chen, J. Xie, Graphene-based heterojunction photocatalysts, Appl. Surf. Sci. 430 (2018) 53–107.
[15] S. Morales-Torres, L.M. Pastrana-Martínez, J.L. Figueiredo, J.L. Faria, A.M.T. Silva, Graphene oxide-P25 photocatalysts for degradation of diphenhydramine pharmaceutical and methyl orange dye, Appl. Surf. Sci. 275 (2013) 361–368.
[16] K.-D. Kim, N.K. Dey, H.O. Seo, Y.D. Kim, D.C. Lim, M. Lee, Photocatalytic decomposition of toluene by nanodiamond-supported TiO_2 prepared using atomic layer deposition, Appl. Catal. A 408 (2011) 148–155.
[17] L.M. Pastrana-Martínez, S. Morales-Torres, S.A.C. Carabineiro, J.G. Buijnsters, J.L. Faria, J.L. Figueiredo, A.M.T. Silva, Nanodiamond-TiO_2 composites for heterogeneous photocatalysis, ChemPlusChem 78 (2013) 801–807.
[18] M.J. Sampaio, L.M. Pastrana-Martinez, A.M.T. Silva, J.G. Buijnsters, C. Han, C.G. Silva, S.A.C. Carabineiro, D.D. Dionysiou, J.L. Faria, Nanodiamond-TiO_2 composites for photocatalytic degradation of microcystin-LA in aqueous solutions under simulated solar light, RSC Adv. 5 (2015) 58363–58370.
[19] H.I. Kim, H.-N. Kim, S. Weon, G.-H. Moon, J.-H. Kim, W. Choi, Robust co-catalytic performance of nanodiamonds loaded on WO_3 for the decomposition of volatile organic compounds under visible light, ACS Catal. 6 (2016) 8350–8360.
[20] Z. Lin, J. Xiao, L. Li, P. Liu, C. Wang, G. Yang, Nanodiamond-embedded p-type copper(I) oxide nanocrystals for broad-spectrum photocatalytic hydrogen evolution, Adv. Energy Mater. 6 (2016) 1501865.
[21] H. Liu, J. Diao, Q. Wang, S. Gu, T. Chen, C. Miao, W. Yang, D. Su, A nanodiamond/CNT-SiC monolith as a novel metal free catalyst for ethylbenzene direct dehydrogenation to styrene, Chem. Commun. 50 (2014) 7810–7812.
[22] J. Diao, Y. Zhang, J. Zhang, J. Wang, H. Liu, D.S. Su, Fabrication of MgO-rGO hybrid catalysts with a sandwich structure for enhanced ethylbenzene dehydrogenation performance, Chem. Commun. 53 (2017) 11322–11325.
[23] V.N. Mochalin, O. Shenderova, D. Ho, Y. Gogotsi, The properties and applications of nanodiamonds, NatureNanotechology 7 (2012) 11–23.
[24] A.M. Schrand, S.A.C. Hens, O.A. Shenderova, Nanodiamond particles: properties and perspectives for bioapplications, Crit. Rev. Solid State Mater. Sci. 34 (2009) 18–74.
[25] A.J. Ramirez, R.A. Brain, S. Usenko, M.A. Mottaleb, J.G. O'Donnell, L.L. Stahl, J.B. Wathen, B.D. Snyder, J.L. Pitt, P. Perez-Hurtado, L.L. Dobbins, B.W. Brooks, C.K. Chambliss, Occurrence of pharmaceuticals and personal care products in fish: results of a national pilot study in the united states, Environ. Toxicol. Chem. 28 (2009) 2587–2597.
[26] C.A. Kinney, E.T. Furlong, S.L. Werner, J.D. Cahill, Presence and distribution of wastewater-derived pharmaceuticals in soil irrigated with reclaimed water, Environ. Toxicol. Chem. 25 (2006) 317–326.
[27] E.S. Elmolla, M. Chaudhuri, Photocatalytic degradation of amoxicillin, ampicillin and cloxacillin antibiotics in aqueous solution using UV/TiO_2 and UV/H_2O_2/TiO_2 photocatalysis, Desalination 252 (2010) 46–52.
[28] S. Brunauer, P.H. Emmett, E. Teller, Adsorption of gases in multimolecular layers, J. Am. Chem. Soc. 60 (1938) 309–319.
[29] A.V. Neimark, Y. Lin, P.I. Ravikovitch, M. Thommes, Quenched solid density functional theory and pore size analysis of micro-mesoporous carbons, Carbon 47 (2009) 1617–1628.
[30] K.B. Holt, D.J. Caruana, E.J. Millán-Barrios, Electrochemistry of undoped diamond nanoparticles: accessing surface redox states, J. Am. Chem. Soc. 131 (2009) 11272–11273.
[31] D. Valerii Yu, Detonation-synthesis nanodiamonds: synthesis, structure, properties and applications, Russ. Chem. Rev. 76 (2007) 339–360.
[32] L.M. Pastrana-Martínez, S. Morales-Torres, V. Likodimos, P. Falaras, J.L. Figueiredo, J.L. Faria, A.M.T. Silva, Role of oxygen functionalities on the synthesis of photocatalytically active graphene–TiO_2 composites, Appl. Catal. B 158–159 (2014) 329–340.
[33] R.J.J. Jansen, H. van Bekkum, XPS of nitrogen-containing functional groups on activated carbon, Carbon 33 (1995) 1021–1027.
[34] T. Jiang, K. Xu, FTIR study of ultradispersed diamond powder synthesized by explosive detonation, Carbon 33 (1995) 1663–1671.
[35] V.L. Kuznetsov, M.N. Aleksandrov, I.V. Zagoruiko, A.L. Chuvilin, E.M. Moroz, V.N. Kolomiichuk, V.A. Likholobov, P.M. Brylyakov, G.V. Sakovitch, Study of ultradispersed diamond powders obtained using explosion energy, Carbon 29 (1991) 665–668.
[36] E. Mironov, A. Koretz, E. Petrov, Detonation synthesis ultradispersed diamond structural properties investigation by infrared absorption, Diam. Relat. Mater. 11 (2002) 872–876.
[37] A.R. Kirmani, W. Peng, R. Mahfouz, A. Amassian, Y. Losovyj, H. Idriss, K. Katsiev, On the relation between chemical composition and optical properties of detonation nanodiamonds, Carbon 94 (2015) 79–84.
[38] Y. Lin, D. Su, Fabrication of nitrogen-modified annealed nanodiamond with improved catalytic activity, ACS Nano 8 (2014) 7823–7833.
[39] O.A. Shenderova, I.I. Vlasov, S. Turner, G. Van Tendeloo, S.B. Orlinskii, A.A. Shiryaev, A.A. Khomich, S.N. Sulyanov, F. Jelezko, J. Wrachtrup, Nitrogen control in nanodiamond produced by detonation shock-wave-assisted synthesis, J. Phys. Chem. C 115 (2011) 14014–14024.
[40] A. Khorsand Zak, W.H. Abd, M.E. Majid, R. Yousefi Abrishami, X-ray analysis of ZnO nanoparticles by Williamson-Hall and size–strain plot methods, Solid State Sci. 13 (2011) 251–256.
[41] A. Krüger, F. Kataoka, M. Ozawa, T. Fujino, Y. Suzuki, A.E. Aleksenskii, A.Y. Vul', E. Ōsawa, Unusually tight aggregation in detonation nanodiamond: identification and disintegration, Carbon 43 (2005) 1722–1730.
[42] R.C. Bansal, J.B. Donnet, F. Stoeckli, Active Carbon, Marcel Dekker, New York, 1988.
[43] O. Shenderova, V. Grichko, S. Hens, J. Walch, Detonation nanodiamonds as UV radiation filter, Diam. Relat. Mater. 16 (2007) 2003–2008.
[44] M. Gärtner, V. Dremov, P. Müller, H. Kisch, Bandgap widening of titania through semiconductor support interactions, ChemPhysChem 6 (2005) 714–718.
[45] N. Brown, O. Hod, Controlling the electronic properties of nanodiamonds via surface chemical functionalization: a DFT study, J. Phys. Chem. C 118 (2014) 5530–5537.
[46] M.E. Kompan, E.I. Terukov, S.K. Gordeev, S.G. Zhukov, Y.A. Nikolaev, Photoluminescence spectra of ultradisperse diamond, Phys. Solid State 39 (1997) 1928–1929.
[47] E. Jimenez-Relinque, I. Llorente, M. Castellote, TiO_2 cement-based materials: understanding optical properties and electronic band structure of complex matrices, Catal. Today 287 (2017) 203–209.
[48] J. Jayabharathi, C. Karunakaran, V. Thanikachalam, P. Ramanathan, Binding and fluorescence enhancing behaviour of phenanthrimidazole with different phases of TiO_2, New J. Chem. 38 (2014) 4321–4335.
[49] C.H. Kim, B.-H. Kim, K.S. Yang, TiO_2 nanoparticles loaded on graphene/carbon composite nanofibers by electrospinning for increased photocatalysis, Carbon 50 (2012) 2472–2481.
[50] N. Serpone, I. Texier, A.V. Emeline, P. Pichat, H. Hidaka, J. Zhao, Post-irradiation effect and reductive dechlorination of chlorophenols at oxygen-free TiO_2/water interfaces in the presence of prominent hole scavengers, J. Photochem. Photobiol., A 136 (2000) 145–155.
[51] C. Minero, G. Mariella, V. Maurino, D. Vione, E. Pelizzetti, Photocatalytic transformation of organic compounds in the presence of inorganic ions. 2. Competitive reactions of phenol and alcohols on a titanium dioxide-fluoride system, Langmuir 16 (2000) 8964–8972.